## PHYSICS

# Observation of exceptional points in magnonic parity-time symmetry devices

Haoliang Liu[1]*, Dali Sun[1,2]*, Chuang Zhang[1], Matthew Groesbeck[1], Ryan Mclaughlin[1], Z. Valy Vardeny[1]†

Non-Hermitian Hamiltonians may still have real eigenvalues, provided that a combined parity-time ($\mathcal{PT}$) symmetry exists. The prospect of $\mathcal{PT}$ symmetry has been explored in several physical systems such as photonics, acoustics, and electronics. The eigenvalues in these systems undergo a transition from real to complex at exceptional points (EPs), where the $\mathcal{PT}$ symmetry is broken. Here, we demonstrate the existence of EP in magnonic devices composed of two coupled magnets with different magnon losses. The eigenfrequencies and damping rates change from crossing to anti-crossing at the EP when the coupling strength increases. The magnonic dispersion includes a strong "acoustic-like" mode and a weak "optic-like" mode. Moreover, upon microwave radiation, the $\mathcal{PT}$ magnonic devices act as magnon resonant cavity with unique response compared to conventional magnonic systems.

## INTRODUCTION

Exceptional points (EPs) (*1–7*), known as degeneracies in non-Hermitian Hamiltonians that possess parity-time ($\mathcal{PT}$) symmetry, have attracted considerable attention because they present a new method to manipulate the energy transfer rate between a system and its environment. In the parameter space, EPs correspond to the transition from real to complex eigenvalues due to symmetry breaking of the non-Hermitian Hamiltonian. $\mathcal{PT}$ symmetry is achieved in photonics when the optical gain and loss in two different device components are carefully balanced (*3*). In these systems, the EPs may be reached by varying the gain/loss ratio or the coupling between the two optical components. The EP creates many intriguing phenomena such as unidirectional invisibility (*8, 9*), loss-induced suppression and revival of lasing (*4, 5*), topological chirality (*10, 11*), and single-mode lasers with gain and loss (*12*). Non-Hermitian physics with devices having variable gain and loss has yielded interesting applications in quantum mechanics (*1*), optomechanics (*13*), superconductivity (*14*), Bose-Einstein condensates (*15*), acoustics (*16*), magnon-photon polaritons (*16–21*), and spintronics (*22–24*). Rather than balancing gain and loss in the two optical components, passive $\mathcal{PT}$ symmetric systems that comprise two components with different optical losses have also been demonstrated in photonics (*4, 25*). Moreover, anti-crossing of eigenfrequencies and manipulated spin current have been observed in the strongly coupled magnon-photon system (*18, 19*).

Recently, $\mathcal{PT}$ symmetry and EPs have been theoretically proposed in the magnon-magnon system at nonequilibrium condition, where the two magnetic layers (say, $i$ and $j$) have balanced magnonic gain and loss (i.e., $\alpha_i = -\alpha_j$) (*22*). The coupled magnonic dynamics is governed by the Landau-Lifshitz-Gilbert (LLG) equations (*26*)

$$\frac{d\mathbf{M}_i}{dt} = -\gamma \mathbf{M}_i \times \mathbf{H}_i - K\gamma \mathbf{M}_i \times \mathbf{M}_j \pm \frac{\alpha_i}{M_j} \mathbf{M}_i \times \frac{d\mathbf{M}_i}{dt} \quad (1)$$

where $\gamma$, $\mathbf{H}_i$, $K$, and $\alpha_i$ are the gyromagnetic ratio, external field, interlayer coupling constant, and Gilbert damping factor, respectively. The

last term in Eq. 1 has either positive or negative $\alpha_i$ ($\alpha_j$) that leads to balanced magnonic loss/gain in the magnetic bilayers. Magnonic loss usually originates from spin-orbit coupling and magnon dissipation, whereas magnonic gain may be achieved by spin-transfer torque (*23*), parametric driving (*22*), and antiferromagnetic skyrmions (*24*). Note that Eq. 1 for $i$ and $j$ is invariant under parity operation, $\mathcal{P}$ ($\mathbf{M}_i \to \mathbf{M}_j$ and $\mathbf{H}_i \to \mathbf{H}_j$), and time reversal, $\mathcal{T}$ ($t \to -t$, $\mathbf{M}_i \mathbf{M}_j \to -\mathbf{M}_i$, and $\mathbf{H}_i \to -\mathbf{H}_i$) [see the Supplementary Materials and (*22*)]. An analytical solution may be obtained when $\mathbf{M}_i = \mathbf{M}_j$ and $\alpha_i = -\alpha_j$, in which the eigenvalues change from real to complex, leading to an EP at a coupling constant $K$ subjected to the relation $(\gamma K M)^2 - (\gamma \alpha)^2 H_{\text{eff}} (H_{\text{eff}} + 2KM) = 0$

There are two obstacles in realizing this condition experimentally. First, the coupling strength in the model was assumed to originate from dipolar interaction that is too weak to achieving $\mathcal{PT}$ symmetry, and second, the Gilbert damping, $\alpha$, can hardly be tuned to be negative (*27*). To overcome these two difficulties, the dipolar interaction between the two magnetic layers should be replaced by the more realistic exchange interaction, which is about two orders of magnitude stronger (*27*). In addition, instead of tuning $\alpha$ for reaching the EP, the exchange interaction between the magnetic layers may be more easily tuned, for example, by changing the distance, $d$, between the magnetic layers. In this case, however, a complication arises because the exchange coupling constant, $J$, alternates with $d$ between positive [ferromagnetic coupling (FC)] and negative [antiferromagnetic coupling (AFC)].

In this work, we demonstrate the existence of EP in a passive magnonic $\mathcal{PT}$ symmetric device in the form of a trilayer structure with two magnetic layers, namely, 30-nm Co and 5-nm NiFe, which are separated by the Pt interlayer, of which thickness, $d$, may be varied. The two different magnetic layers have different Gilbert damping, $\alpha$, a situation that is similar to a passive $\mathcal{PT}$ symmetric system in photonics. We show that by increasing $d$, the exchange interaction between the magnetic layers diminishes while alternating between FC and AFC. The EP is reached in this system by increasing the coupling strength to a critical value, $J_c$, where the real parts of the eigenvalues (i.e., the resonant frequencies) change from crossing to anti-crossing, comparable with the magnon-photon system. In addition, we show that microwave (MW) photon dissipation and magnon gain are more efficient in the $\mathcal{PT}$ symmetric magnon system before reaching saturation at the EP.

[1]Department of Physics and Astronomy, University of Utah, Salt Lake City, UT 84112, USA. [2]Department of Physics, North Carolina State University, Raleigh, NC 27695, USA.
*These authors contributed equally to this work.
†Corresponding author. Email: val@physics.utah.edu

## RESULTS

### Model for passive magnonic $\mathcal{PT}$ symmetry

Figure 1A shows the schematics of a passive magnonic $\mathcal{PT}$ symmetry system. The two magnetic layers are separated by a nonmagnetic layer and have FC/AFC exchange coupling, $J$, depending on the interlayer thickness. It is seen that the eigenfrequencies and damping constants of the collective magnetic moment dynamics are modulated when changing $J$, leading to a dispersive response. In our calculation, we have used a simple model to obtain the system eigenmodes based on two LLG equations (see Eq. 1 and the Supplementary Materials for details) (22). Figure 1B shows the obtained eigenfrequencies and Gilbert damping of the collective magnetic moment dynamics in the trilayer as a function of $J$, where the two magnetic layers have identical magnetizations but opposite Gilbert damping, $\alpha_0$. The parameters were chosen to describe two identical cobalt films in the trilayer at an external in-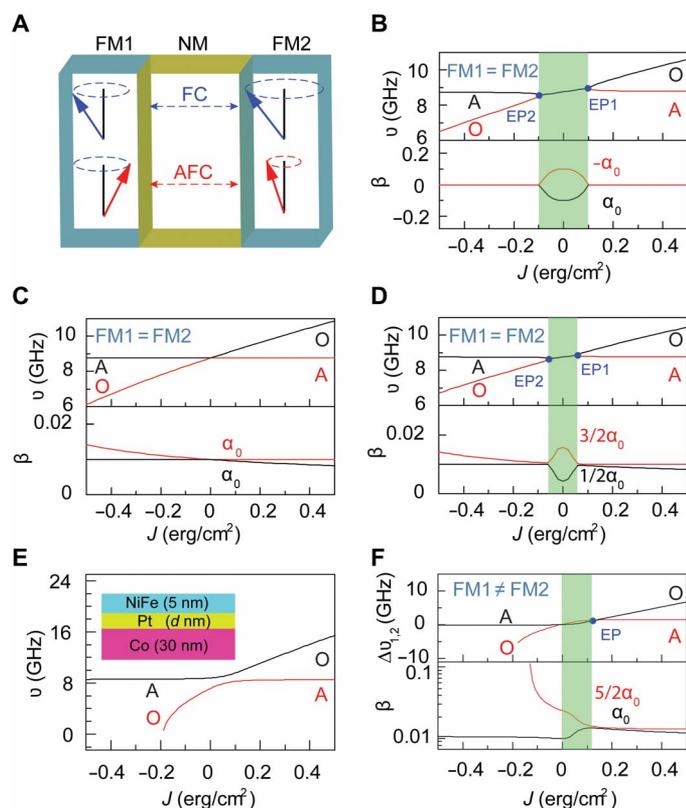plane magnetic field, $B = 700$ G. It is seen that with increasing $J$, the two eigenfrequencies, $\nu_1$ and $\nu_2$, bifurcate at a critical exchange, $J_c$, forming an EP that corresponds to the transition from $\mathcal{PT}$ symmetric regime to a $\mathcal{PT}$ broken phase. Simultaneously, the relative damping constants $\beta = -\mathrm{Im}(\nu)/\mathrm{Re}(\nu)$ of the two magnetic layers decrease together and, at $J_c$, merge at $\beta = 0$. We note that EP occurs at $J_c$ and $-J_c$, resulting in two EPs (Fig. 1B). Moreover, in the $\mathcal{PT}$ broken regime ($J > J_c$), there are two eigenfrequency branches, namely, a low-frequency acoustic mode (A; in phase) and a high-frequency optical mode (O; out of phase) (26).

Figure 1C shows the calculated eigenfrequencies with $J$ in the same trilayer device, where the magnetic (Co) layers have the same damping constant, $\alpha_0$. In this case, the eigenfrequencies coalesce only at $J = 0$, where the acoustic and optical modes exchange their roles. Note that, here, there are no EPs and no $\mathcal{PT}$ symmetry broken phase in this case. Figure 1D shows the calculated eigenfrequencies with $J$, where the two Co layers have the same magnetization but different $\alpha_0$ ($>0$); this corresponds to the passive $\mathcal{PT}$ symmetry case. In contrast to the case shown in Fig. 1C, here, the eigenfrequencies versus $J$ response is similar to that in Fig. 1B, except that the $\mathcal{PT}$ symmetric phase in $J$ is smaller, and for $J > J_c$, a weak optical mode appears (see fig. S2) in addition to the dominant acoustic mode. The eigenfrequency imaginary part has a constant background of $\alpha_0$, which is different than the zero background in Fig. 1C. Similar to passive $\mathcal{PT}$ symmetry in photonics (25), we can deduce that the $\mathcal{PT}$ symmetry is reestablished in passive magnonic $\mathcal{PT}$ symmetry based on the analytical solutions (see eqs. S3 and S4). We therefore conclude that to experimentally study magnonic $\mathcal{PT}$ symmetry and EPs, we do not need to induce magnetic gain where $\alpha_0 < 0$, but instead, we may use magnets with different $\alpha_0$ to achieve passive $\mathcal{PT}$ symmetric structures; this trilayer can be readily fabricated using two different magnetic layers.

Figure 1 (E and F) shows the calculated eigenfrequencies and damping rate response in a trilayer that consists of 30-nm Co ($\alpha_0 = 0.0103$) and 5-nm NiFe ($\alpha_0 = 0.0250$), which are suitable to our experiments (see below). The eigenfrequencies show acoustic and optical modes at large $J$ and get close to each other at small $J$ (Fig. 1E and fig. S2). To compare the frequency response with $J$ to that in Fig. 1D, where the two ferromagnets (FMs) are the same but have different $\alpha_0$, we subtract from the obtained eigenfrequencies the eigenfrequencies, $\nu_{0,i}$, of each individual FM layer without coupling strength (Fig. 1F). Following this modification, the two obtained "difference frequencies" $\Delta\nu_1$ ($= \nu_1 - \nu_{0,1}$) and $\Delta\nu_2$ ($= \nu_2 - \nu_{0,2}$) branches evolve with $J$ from crossing to anticrossing and can be better compared with Fig. 1D, where the EP can be readily determined at $J > 0$. At the same conditions, the damping rate responses versus $J$ show acoustic and optical modes for $J > J_c$, which are not symmetric in the regimes of $J > 0$ and $J < 0$ because of the asymmetry of the two different magnetic layers.

### Experimental evidence for EPs in passive magnonic $\mathcal{PT}$ symmetry

To verify the passive $\mathcal{PT}$ symmetry model experimentally, we measured the eigenfrequencies and damping rates of the collective dynamics in trilayers that consist of coupled 30-nm Co and 5-nm NiFe magnetic films separated by a nonmagnetic Pt interlayer of various thicknesses, $d$. We used three different techniques, which are broadband ferromagnetic resonance (FMR) (28), Brillouin light scattering (BLS), and magneto-optical Kerr effect (MOKE), as described in Materials and Methods.

For the FMR, the field derivative of the MW absorption at a fixed MW frequency, $\nu$, has been recorded while sweeping the applied
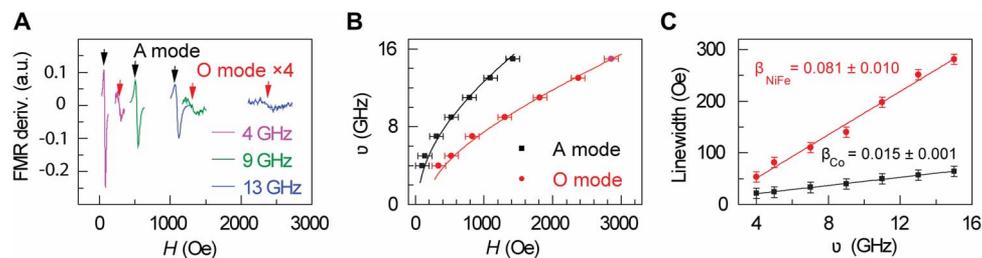


**Fig. 1. Theoretical model for magnonic passive $\mathcal{PT}$ symmetric system.** (**A**) Schematic structure of a trilayer system, where the two coupled ferromagnet (FM) layers are separated by a nonmagnetic (NM) layer. The coupling strength can be tuned by varying the nonmagnetic (NM) layer thickness. (**B** to **D**) Calculated eigenfrequencies and damping rates of the magnonic trilayer system for the following conditions: (B) One Co layer (FM1) has positive Gilbert damping $\alpha_1 = \alpha_0 = 0.01$, whereas the second Co layer (FM2) has negative $\alpha_2 = -\alpha_0$ (equal to −0.01). (C) Both Co layers have $\alpha_1 = \alpha_2 = \alpha_0$. (D) One Co layer has $\alpha_1 = 3/2\alpha_0$ (equal to 0.015), whereas the second Co layer has $\alpha_2 = 1/2\alpha_0$ (equal to 0.005). (**E**) Calculated eigenfrequencies with Co and NiFe FM layers separated by a Pt interlayer. Inset: Schematics of the $\mathcal{PT}$ symmetric trilayer. (**F**) Same as in (E) but for the eigenfrequency changes (top) after subtracting the eigenfrequencies of the corresponding FM with no coupling. The corresponding damping constants are given in the bottom panel. Here, the unperturbed Gilbert damping constants of Co and NiFe are $\alpha_1 = \alpha_0$ and $\alpha_2 = 5/2\alpha_0$, respectively.

**Fig. 2. Determination of the eigenfrequencies and Gilbert damping constants in a magnonic $\mathcal{PT}$ symmetric trilayer by FMR measurements.** (**A**) Derivative of the MW absorption of a Co (30 nm)/Pt (2.4 nm)/NiFe (5 nm) trilayer at FMR conditions, measured at several MW frequencies, ν. The Co-like acoustic (A) and NiFe-like optical (O) magnonic modes are assigned. a.u., arbitrary units. (**B**) Resonant fields of the two magnonic modes at various MW frequencies. The solid curves are fitted by the Kittel equation with parameters given in the text. (**C**) Linewidths of the two magnonic modes as a function of the MW frequencies. The solid lines are linear fits to help obtain the Gilbert damping constants.
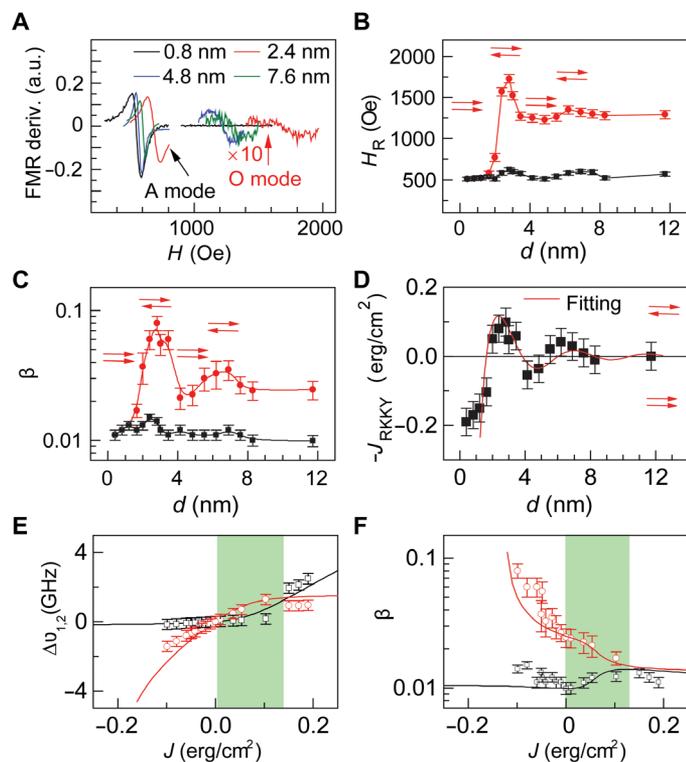


**Fig. 3. Experimental verification of the magnonic $\mathcal{PT}$ symmetric system using broadband FMR measurements.** (**A**) Two magnonic modes, namely, acoustic (A) and optical (O), in trilayers of various Pt interlayer thicknesses, d, measured at MW frequency of 9 GHz. (**B**) Resonance fields of the two magnonic modes as a function of the Pt interlayer thickness. (**C**) Gilbert damping rates of the two magnonic modes obtained at various d values. (**D**) RKKY exchange constant, $J_{RKKY}$, versus d obtained from (B) using the Kittel equation (see text). The solid line through the data points is calculated from a phenomenological model of the RKKY exchange interaction. (**E**) Magnon eigenfrequency changes, $\Delta\nu = \nu - \nu_0$ (ν is for the obtained eigenfrequency and $\nu_0$ is for the unperturbed FMR frequency), of several trilayers plotted as a function of the coupling strength, $J_{RKKY}$. (**F**) Gilbert damping constants plotted against $J_{RKKY}$. The lines through the data points in (E) and (F) are a fit using the $\mathcal{PT}$ symmetry model shown in Fig. 1F. The green area indicates the parameter domain of the passive $\mathcal{PT}$ symmetry.

magnetic field, H. Figure 2A shows FMR (H) response at different MW frequencies for a trilayer with Pt interlayer thickness d = 2.4 nm, which is in the strong coupling regime. Two resonances are observed at each ν with large and small amplitudes, respectively, which corre-

spond to two eigenmodes of the magnonic structure; these are the strong acoustic (in-phase magnetization precession) and weak optic (out-of-phase precession) modes, respectively (29). The relation that determines the resonance field, $H_{eff}$, at fixed ν may be derived by the Kittel formula (26), $\nu = \gamma \sqrt{H_{eff}(H_{eff} + 4\pi M_{eff})} H_{eff}$, where γ, $H_{eff}$, and $M_{eff}$ are the gyromagnetic ratio, effective field, and effective magnetization, respectively. The effective field $H_{eff} = H_0 + H_{ex}$ is a combination of the external field, $H_0$, and exchange coupling field, $H_{ex}$. Using the Kittel formula, we could readily fit the resonance fields of the acoustic and optical magnonic branches as a function of magnetic field, as shown in Fig. 2B. From the fitting, we obtained the parameters $H_{ex}$ and $M_{eff}$ from which the exchange coupling constant $J_{RKKY}$ is defined as $H_{ex} = \frac{J_{RKKY}}{M_{eff}d}$.

The frequency dependencies of the FMR linewidth for the acoustic and optical modes are shown in Fig. 2C; both FMR responses broaden with ν. These dependencies can be fitted by the linear relation $\Delta H = \Delta H_0 + \frac{4\pi \alpha \nu}{\sqrt{3}\gamma}$, where $\Delta H_0$ is the inhomogeneous FMR broadening due to structural imperfections in the FM film and α is the Gilbert damping factor. From the linear responses in Fig. 2C, at large d, we obtained $\alpha_0(Co) = 0.015$ and $\alpha_0(NiFe) = 0.081$. This is in agreement with the relative weak strengths of the optical resonance (NiFe-like; large damping) and the relative strong strengths of acoustic resonance (Co-like; small damping).

Figure 3A shows the FMR response of the trilayer structures with various Pt interlayer thicknesses at fixed MW frequency of 9 GHz. As seen in Fig. 3B, the resonance fields of the two modes oscillate with d, indicating that they are determined by the J sign change between FC and AFC interactions. Figure 3C shows the damping constant, β, of the two resonance modes at various d, which also oscillates with the Pt interlayer thickness. It should be stressed that an acoustic mode only exists when the interlayer coupling strength surpasses the EP (see Fig. 3A with d = 0.8 nm), whereas the optical mode is suppressed, although there are still two mathematical solutions, which is consistent with the general situation for a second-order EP in $\mathcal{PT}$ symmetry systems (25).

Figure 3D shows the calculated exchange coupling constants, $J_{RKKY}$, obtained from the fitting of the trilayer resonance frequencies at various d. $J_{RKKY}(d)$ response may be well fitted by the Ruderman-Kittel-Kasuya-Yosida (RKKY) model interaction (30): $J_{RKKY} \sim \sin\left(\theta + \frac{2\pi d}{\lambda_F}\right)/d^n$, which shows a decaying oscillatory behavior with d. From the RKKY fit to the extracted J(d) response, we determined the Pt Fermi wavelength, $\lambda_F$, to be $\lambda_F = 4.1 \pm 0.4$ nm, which is slightly larger than that found in the bulk (31), whereas we found $n = 1.8 \pm 0.2$, in good agreement with previous theoretical predictions (30).
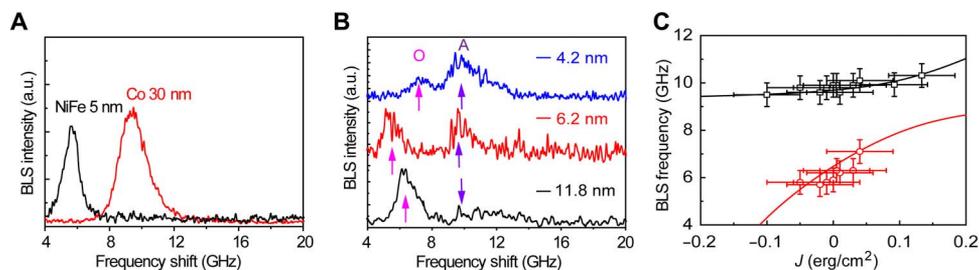
**Fig. 4. BLS of magnons in $\mathcal{PT}$ symmetry trilayers of Co/Pt/NiFe.** (**A**) BLS spectra of Damon-Eschbach–type magnons in unperturbed films of Co (30 nm) and NiFe (5 nm), measured at an in-plane applied magnetic field of 750 G (shown for reference). (**B**) Typical BLS spectra of magnons in trilayers with different Pt thickness, $d$, as given. The respective arrows point to the acoustic (pink) and optical (blue) modes. (**C**) Obtained magnon frequencies in the trilayers plotted against the interlayer coupling constant, $J$. The solid lines are calculated magnon eigenfrequencies of A and O modes based on our $\mathcal{PT}$ symmetry model (Fig. 1).

We also note that the RKKY interaction is also verified from the MOKE hysteresis loop measurements using the Sagnac interferometer (see fig. S3). We note that our system is different from the conventional spin-valve trilayer structure because Pt has the strongest spin-orbit coupling and the shortest spin diffusion length among nonmagnetic metals, and consequently, spin current transport and dynamic exchange coupling between the two FM layers are effectively suppressed (*32*). In our model, we neglected the contribution of the dynamic exchange coupling, but it may contribute to the damping change at very small Pt interlayer thicknesses.

To compare our experimental results to the model calculation, we have done the following modifications to the data presentation. First, on the basis of the values of the extracted exchange coupling constants, $J_{RKKY}$, at each $d$ value, we replotted Fig. 3 (B and C) in terms of $J_{RKKY}$, as seen in Fig. 3 (E and F). In addition, we also converted the resonance fields at a fixed MW frequency into eigenfrequencies using the Kittel equation at a fixed magnetic field of 700 G. Upon doing these modifications, it becomes clear that the experimentally determined trilayer eigenfrequencies and damping constants follow the theoretical model presented in Fig. 1F in both parameter regimes, namely, the passive $\mathcal{PT}$ symmetry and broken $\mathcal{PT}$ symmetry. The two branches of eigenfrequencies cross each other at the EP. The agreement between the data and model calculation shows that the $\mathcal{PT}$ symmetry physics also exists in magnonics, which is a field that this behavior needed proving.

Magnons can also be directly characterized by the BLS technique, which is very sensitive to various magnon types that include uniform and nonuniform modes in FM systems (*28*). The room temperature BLS spectra of the passive magnonic $\mathcal{PT}$ symmetric devices measured at a fixed magnetic field of $B \sim 750$ G are shown in Fig. 4. Figure 4A shows the BLS spectra of reference samples, namely, 30-nm Co and 5-nm NiFe; their obtained magnon frequencies obey the Kittel equation. Figure 5B shows the BLS spectra in the trilayer devices with various Pt thicknesses. Note that the larger noise level in Fig. 5B is due to less experimental average time. Both the Co-like/acoustic mode and NiFe-like/optic mode frequencies and intensities change when varying $d$, as summarized in Fig. 5C. Here, we transformed the $d$ values into $J$ values, using our previous analysis summarized above; the responses are well fitted by our model. It should be stressed that the two modes merge together at small $d$ values close to the EP in this system. In addition, we have recognized a group of new magnons that emerges at low frequencies under MW irradiation (see figs. S5 and S6).

## Detection of nonequilibrium magnons in the trilayer devices

We have also investigated nonequilibrium magnons in the passive magnonic $\mathcal{PT}$ symmetric devices that are driven by MW radiation
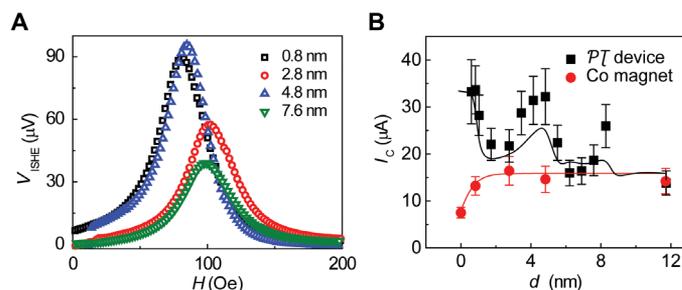


**Fig. 5. Nonequilibrium magnon current detection in $\mathcal{PT}$ symmetry trilayers via the ISHE in a Pt overlayer.** (**A**) Typical ISHE voltage generated at magnetic field close to the acoustic magnon mode (Co-like) in trilayers of different Pt thicknesses, as given. (**B**) Generated ISHE electric current (black squares) as a function of the Pt thickness, $d$. The black solid line is calculated on the basis of fig. S2E and eqs. S6 and S7. The red circles are the obtained ISHE current for conventional Co (30 nm)/Pt ($x$ nm) bilayers shown for reference, where the red solid line is calculated from eq. S6.

at FMR conditions. The magnonic device absorbs MW photons and excites coherent magnon current, which flows from the magnonic device into a nonmagnetic overlayer that forms a magnon sink that is attached to the device. The magnon current can then be converted via the spin-orbit interaction into charge current in the nonmagnetic layer by the inverse spin Hall effect (ISHE) (*33*). To detect the MW-generated magnon current in a passive magnonic $\mathcal{PT}$ symmetric device, a 7-nm Pt film was deposited onto the trilayer structures that serve as a detector layer via the ISHE (*28*).

Figure 5A shows the ISHE voltage responses $V_{ISHE}(H)$ generated in the external Pt layer by the strong acoustic magnon modes (Co-like band) in several trilayers with various $d$'s that are detected in the Pt overlayer. It is seen that $V_{ISHE}(H)$ varies with $d$ despite the fact that the MW excitation power stays constant. Figure 5B shows the ISHE current, $I_{ISHE}$, as a function of the interlayer thicknesses $d$, normalized by the sheet resistance of the Pt overlayer (see fig. S5), which is proportional to the magnon current. Compared with $V_{ISHE}$ (red circle points) detected in conventional magnet Co with various $d$'s, it is seen that $V_{ISHE}$ generated by the trilayer structures is always larger (in both FC and AFC regimes), and it reaches saturation after surpassing the EP (see also fig. S2E). The fit to $V_{ISHE}(d)$ seen in Fig. 5B well reproduces the data (see theory part in the Supplementary Materials). The experimental results and fitting demonstrate that passive magnonic $\mathcal{PT}$ symmetric device can absorb more MW photons and generate nonequilibrium magnon current more efficiently compared with conventional magnets before reaching broken $\mathcal{PT}$ symmetric phase.

## DISCUSSION

In summary, we have demonstrated the existence of an EP in a passive magnonic $\mathcal{PT}$ symmetry system of trilayers composed of Co (30 nm)/Pt ($d$ nm)/NiFe (5 nm) with various $d$'s. The EP is reached by tuning the RKKY-type coupling strength between the Co and NiFe magnetic layers when varying $d$. Similar to the magnon-photon system, the eigenfrequencies of the magnonic system change from crossing to anti-crossing at the EP. In addition, the passive $\mathcal{PT}$ symmetric magnonic device can more efficiently absorb MW photons and thus generate more magnons upon MW irradiation, which may be transformed into larger current via the ISHE.

Our work initiates the $\mathcal{PT}$ symmetry applications in the field of magnonics. Our previously unidentified magnonic $\mathcal{PT}$ symmetric device has practical applications in three different avenues: First, the magnetic damping of materials can be tuned in our device, which is very important in the design of new information processing technology–magnonic circuit. Second, the nonequivalent magnon current can be efficiently excited and translated into electric current, which benefits the magnon-spintronic device applications. Last, we notice that the $\mathcal{PT}$ symmetric magnonic bilayer has been recently theoretically proposed as an ultra-sensitive magnetometer (34). Our device could serve as an experimental verification of the theoretical predictions because, at the EP, the eigenfrequency changes of the two largely different magnets coalesce. This EP state has high sensitivity to external perturbations of gain changes such as MW photon irradiation and electric current injection.

## MATERIALS AND METHODS
### The trilayer fabrication
The trilayer structures were prepared on Si (100) wafer with a 4-nm $Si_3N_4$ buffer layer. The thin films of Co, Pt, and $Ni_{80}Fe_{20}$ were grown by e-beam evaporation at deposition rates of 0.05, 0.02, and 0.1 nm/s, respectively, in a high-vacuum deposition chamber (Angstrom Engineering Inc.). The base pressure was $3 \times 10^{-8}$ mbar. Before taking the devices out of the chamber, they were capped with 100-nm $SiO_2$ as a protective layer.

### The Sagnac MOKE
Because a rotation of the plane of polarization of linearly polarized light can be equivalently described as a phase shift between two circular polarizations of light, an interferometry scheme has been used to measure the phase shift with higher accuracy and stability than conventional MOKE detection schemes. A linearly polarized coherent light source centered at 1550 nm was first split into two orthogonal linear polarized beams of equal power and then converted into right/left circular polarization by a quarter-wave plate (QWP) before reflecting from the sample. The beams were allowed to pass through the QWP once more to convert back to a linear polarization before reaching a photodetector, where an interference pattern is observed. The relative phase between the two beams was measured by a lock-in amplifier, and the Kerr rotation angle was obtained from the phase shift.

### Broadband FMR measurements
The measurements were performed at room temperature using a co-planar waveguide design. The MW excitation was generated by an Agilent N5173B source with a frequency range of 9 KHz to 20 GHz. The samples were installed on top of the MW guide of a 250-μm-wide signal transmission line with radio frequency magnetic field perpendicular to a dc magnetic field. The insulation between the NiFe layer and MW signal transmission was guaranteed by 100-nm $SiO_2$. The FMR responses were obtained by sweeping the dc magnetic field at each MW frequency. The MW power was kept at 10 dBm during the measurements. The transmission signal was detected by a phase-sensitive technique with modulation of a small ac magnetic field (86 Hz, 20 Oe) realized by a Helmholtz coil placed between the poles of the dc magnet. The Gilbert damping factors were obtained by averaging the results from three different samples with the same Pt thickness.

### Brillouin light scattering
The BLS measurements were carried out using a Sandercock-type six-pass tandem Fabry-Perot interferometer in a backscattering geometry. The P-polarized excitation beam of ~50-mW power was extracted from a single-mode solid-state laser that operated at a wavelength of 532 nm. The applied dc magnetic field was perpendicular to the incident plane of light, which corresponds to the Damon-Eschbach spin-wave configuration.

### Inverse spin Hall effect
The MW frequency of 4 GHz was amplified using an amplifier (range, 3 to 4 GHz) with a maximum output of ~100 mW. The samples with inverted trilayer structures were placed on an MW guide transmission line. The insulation between the Co and MW transmission was guaranteed by 100-nm $SiO_2$. The ISHE voltage was generated in a 7-nm Pt overlayer and detected by a phase-sensitive technique, where the MW was modulated by a square wave at 17 kHz.

## SUPPLEMENTARY MATERIALS
Supplementary material for this article is available at http://advances.sciencemag.org/cgi/content/full/5/11/eaax9144/DC1
Section S1. Theoretical model of $\mathcal{PT}$ symmetry in trilayer structure
Section S2. RKKY interaction characterized by MOKE measurements using Sagnac interferometer
Section S3. Dynamic detection of magnon current using the ISHE
Section S4. Magnon modes in the $\mathcal{PT}$ symmetric trilayer measured by Brillouin light scattering
Fig. S1. The geometry used in theoretical model calculation for the magnonic passive $\mathcal{PT}$ symmetric system.
Fig. S2. Calculated FMR absorption of the magnonic passive $\mathcal{PT}$ symmetric system at different interlayer coupling strengths.
Fig. S3. Characterization of the RKKY exchange interaction in the trilayer devices measured by MOKE using a Sagnac interferometer.
Fig. S4. The magnetization values associated to the two collective modes obtained from the broadband FMR results using the Kittel equation.
Fig. S5. Conversion of the magnonic current into electric current in various trilayer devices capped with a 7-nm Pt detection layer.
Fig. S6. Determination of magnon frequencies in the magnonic trilayer devices.
Fig. S7. BLS spectrum of magnon modes upon MW radiation in a trilayer close to an EP.
References (35–39)

## REFERENCES AND NOTES
1. C. M. Bender, S. Boettcher, Real spectra in non-Hermitian Hamiltonians having PT symmetry. *Phys. Rev. Lett.* **80**, 5243–5246 (1998).
2. R. El-Ganainy, K. G. Makris, M. Khajavikhan, Z. H. Musslimani, S. Rotter, D. N. Christodoulides, Non-Hermitian physics and PT symmetry. *Nat. Phys.* **14**, 11–19 (2018).
3. H. Hodaei, M.-A. Miri, M. Heinrich, D. N. Christodoulides, M. Khajavikhan, Parity-time–symmetric microring lasers. *Science* **346**, 975–978 (2014).
4. A. Guo, G. J. Salamo, D. Duchesne, R. Morandotti, M. Volatier-Ravat, V. Aimez, G. A. Siviloglou, D. N. Christodoulides, Observation of *PT*-symmetry breaking in complex optical potentials. *Phys. Rev. Lett.* **103**, 093902 (2009).
5. M. A. Bandres, S. Wittek, G. Harari, M. Parto, J. Ren, M. Segev, D. N. Christodoulides, M. Khajavikhan, Topological insulator laser: Experiments. *Science* **359**, 1231 (2018).

6. M. B. Carl, Making sense of non-Hermitian Hamiltonians. *Rep. Prog. Phys.* **70**, 947 (2007).

7. W. D. Heiss, The physics of exceptional points. *J. Phys. A Math. Theor.* **45**, 444016 (2012).

8. Z. Lin, H. Ramezani, T. Eichelkraut, T. Kottos, H. Cao, D. N. Christodoulides, Unidirectional invisibility induced by PT-symmetric periodic structures. *Phys. Rev. Lett.* **106**, 213901 (2011).

9. B. Peng, Ş. K. Özdemir, F. Lei, F. Monifi, M. Gianfreda, G. L. Long, S. Fan, F. Nori, C. M. Bender, L. Yang, Parity–time-symmetric whispering-gallery microcavities. *Nat. Phys.* **10**, 394–398 (2014).

10. J. Doppler, A. A. Mailybaev, J. Böhm, U. Kuhl, A. Girschik, F. Libisch, T. J. Milburn, P. Rabl, N. Moiseyev, S. Rotter, Dynamically encircling an exceptional point for asymmetric mode switching. *Nature* **537**, 76–79 (2016).

11. H. Xu, D. Mason, L. Jiang, J. G. E. Harris, Topological energy transfer in an optomechanical system with exceptional points. *Nature* **537**, 80–83 (2016).

12. L. Feng, Z. J. Wong, R.-M. Ma, Y. Wang, X. Zhang, Single-mode laser by parity-time symmetry breaking. *Science* **346**, 972–975 (2014).

13. X.-Y. Lü, H. Jing, J.-Y. Ma, Y. Wu, PT-symmetry-breaking chaos in optomechanics. *Phys. Rev. Lett.* **114**, 253601 (2015).

14. J. Rubinstein, P. Sternberg, Q. Ma, Bifurcation diagram and pattern formation of phase slip centers in superconducting wires driven with electric currents. *Phys. Rev. Lett.* **99**, 167003 (2007).

15. E. M. Graefe, H. J. Korsch, A. E. Niederle, Mean-field dynamics of a Non-Hermitian Bose-Hubbard dimer. *Phys. Rev. Lett.* **101**, 150408 (2008).

16. R. Fleury, D. Sounas, A. Alù, An invisible acoustic sensor based on parity-time symmetry. *Nat. Commun.* **6**, 6905 (2015).

17. Ö. O. Soykal, M. E. Flatté, Strong field interactions between a nanomagnet and a photonic cavity. *Phys. Rev. Lett.* **104**, 077202 (2010).

18. D. Zhang, X.-Q. Luo, Y.-P. Wang, T.-F. Li, J. Q. You, Observation of the exceptional point in cavity magnon-polaritons. *Nat. Commun.* **8**, 1368 (2017).

19. L. Bai, M. Harder, P. Hyde, Z. Zhang, C. Hu, Cavity mediated manipulation of distant spin currents using a cavity-magnon-polariton. *Phys. Rev. Lett.* **118**, 217201 (2017).

20. G.-Q. Zhang, J. Q. You, Higher-order exceptional point in a cavity magnonics system. *Phys. Rev. B* **99**, 054404 (2019).

21. P. Hyde, B. M. Yao, Y. S. Gui, G.-Q. Zhang, J. Q. You, C.-M. Hu, Direct measurement of foldover in cavity magnon-polariton systems. *Phys. Rev. B* **98**, 174423 (2018).

22. J. M. Lee, T. Kottos, B. Shapiro, Macroscopic magnetic structures with balanced gain and loss. *Phys. Rev. B* **91**, 094416 (2015).

23. A. Galda, V. M. Vinokur, Parity-time symmetry breaking in magnetic systems. *Phys. Rev. B* **94**, 020408 (2016).

24. H. Yang, C. Wang, T. Yu, Y. Cao, P. Yan, Antiferromagnetism emerging in a ferromagnet with gain. *Phys. Rev. Lett.* **121**, 197201 (2018).

25. L. Feng, Y. L. Xu, W. S. Fegadolli, M. H. Lu, J. E. B. Oliveira, V. R. Almeida, Y. F. Chen, A. Scherer, Experimental demonstration of a unidirectional reflectionless parity-time metamaterial at optical frequencies. *Nat. Mater.* **12**, 108–113 (2013).

26. C. Kittel, On the theory of ferromagnetic resonance absorption. *Phys. Rev.* **73**, 155–161 (1948).

27. S. Chikazumi, *Physics of Ferromagnetism* (Oxford Univ. Press, ed. 2, 1997).

28. H. Liu, C. Zhang, H. Malissa, M. Groesbeck, M. Kavand, R. McLaughlin, S. Jamali, J. Hao, D. Sun, R. A. Davidson, L. Wojcik, J. S. Miller, C. Boehme, Z. V. Vardeny, Organic-based magnon spintronics. *Nat. Mater.* **17**, 308–312 (2018).

29. C. He, G. Yu, C. Grezes, J. Feng, Z. Zhao, S. A. Razavi, Q. Shao, A. Navabi, X. Li, Q. L. He, M. Li, J. Zhang, K. L. Wong, D. Wei, G. Zhang, X. Han, P. K. Amiri, K. L. Wang, Spin-torque ferromagnetic resonance in W/Co-Fe-B/W/Co-Fe-B/MgO stacks. *Phys. Rev. Appl.* **10**, 034067 (2018).

30. S. S. P. Parkin, D. Mauri, Spin engineering: Direct determination of the Ruderman-Kittel-Kasuya-Yosida far-field range function in ruthenium. *Phys. Rev. B* **44**, 7131–7134 (1991).

31. H. Stanislaw, D. Tomasz, Work functions of elements expressed in terms of the Fermi energy and the density of free electrons. *J. Phys. Condens. Matter* **10**, 10815 (1998).

32. B. Heinrich, Y. Tserkovnyak, G. Woltersdorf, A. Brataas, R. Urban, G. E. W. Bauer, Dynamic exchange coupling in magnetic bilayers. *Phys. Rev. Lett.* **90**, 187601 (2003).

33. E. Saitoh, M. Ueda, H. Miyajima, G. Tatara, Conversion of spin current into charge current at room temperature: Inverse spin-Hall effect. *Appl. Phys. Lett.* **88**, 182509 (2006).

34. Y. Cao, P. Yan, Exceptional magnetic sensitivity of PT-symmetric cavity magnon polaritons. *Phys. Rev. B* **99**, 214415 (2019).

35. R. J. Hicken, C. Daboo, M. Gester, A. J. R. Ives, S. J. Gray, J. A. C. Bland, Interlayer exchange coupling in epitaxial Fe/Cr/Fe/Ag/GaAs(100) structures. *J. Appl. Phys.* **78**, 6670–6678 (1995).

36. A. Bardasis, D. S. Falk, R. A. Ferrell, M. S. Fullenbaum, R. E. Prange, D. L. Mills, Possibility of long-range spin polarization in a degenerate electron gas. *Phys. Rev. Lett.* **14**, 298–300 (1965).

37. K. Ando, S. Takahashi, J. Ieda, Y. Kajiwara, H. Nakayama, T. Yoshino, K. Harii, Y. Fujikawa, M. Matsuo, S. Maekawa, E. Saitoh, Inverse spin-Hall effect induced by spin pumping in metallic system. *J. Appl. Phys.* **109**, 103913 (2011).

38. P. Grünberg, R. Schreiber, Y. Pang, M. B. Brodsky, H. Sowers, Layered magnetic structures: Evidence for antiferromagnetic coupling of Fe layers across Cr interlayers. *Phys. Rev. Lett.* **57**, 2442–2445 (1986).

39. A. Haldar, C. Banerjee, P. Laha, A. Barman, Brillouin light scattering study of spin waves in NiFe/Co exchange spring bilayer films. *J. Appl. Phys.* **115**, 133901 (2014).

# Science Advances

## Observation of exceptional points in magnonic parity-time symmetry devices

Haoliang Liu, Dali Sun, Chuang Zhang, Matthew Groesbeck, Ryan Mclaughlin and Z. Valy Vardeny

| | |
|---|---|
| **ARTICLE TOOLS** | http://advances.sciencemag.org/content/5/11/eaax9144 |
| **SUPPLEMENTARY MATERIALS** | http://advances.sciencemag.org/content/suppl/2019/11/18/5.11.eaax9144.DC1 |
| **REFERENCES** | This article cites 38 articles, 2 of which you can access for free<br>http://advances.sciencemag.org/content/5/11/eaax9144#BIBL |
| **PERMISSIONS** | http://www.sciencemag.org/help/reprints-and-permissions |

Use of this article is subject to the Terms of Service